An Analysis of the Effects of Clouds in High-Resolution Forecasting of Surface Shortwave Radiation in South Africa

JOANA MENDES,[a] NOSIPHO ZWANE,[b] BRIGHTON MABASA,[b] HENERICA TAZVINGA,[b] KAREN WALTER,[a] CYRIL J. MORCRETTE,[a,c,d] AND JOEL BOTAI[e]

[a] *Met Office, Exeter, United Kingdom*
[b] *South African Weather Service, Pretoria, South Africa*
[c] *Department of Mathematics and Statistics, University of Exeter, Exeter, United Kingdom*
[d] *Global Systems Institute, University of Exeter, Exeter, United Kingdom*
[e] *Department of Geography, Geoinformatics and Meteorology, University of Pretoria, Pretoria, South Africa*

(Manuscript received 28 March 2023, in final form 15 November 2023, accepted 17 November 2023)

ABSTRACT: We assess site-specific surface shortwave radiation forecasts from two high-resolution configurations of the South African Weather Service numerical weather prediction model, at 4 and 1.5 km. The models exhibit good skill overall in forecasting surface shortwave radiation, with zero median error for all radiation components. This information is relevant to support a growing renewable energy sector in South Africa, particularly for photovoltaics. Further model performance analysis has shown an imbalance between cloud and solar radiation forecasting errors. In addition, cloud overprediction does not necessarily equate to underestimating solar radiation. Overcast cloud regimes are predicted too often with an associated positive mean radiation bias, whereas the relative abundance of partly cloudy regimes is underpredicted by the models with mixed radiation biases. Challenges highlighted by the misrepresentation of partly cloudy regimes in solar radiation error attribution may be used to inform improvements to the numerical core, namely, the cloud and radiation schemes.

SIGNIFICANCE STATEMENT: This paper provides the first comprehensive assessment of high-resolution site-specific NWP forecasts of surface shortwave radiation in South Africa, exploring clouds as the main drivers of prediction biases. Error attribution analyses of this kind are close to none for this part of the world. Our study contributes to understanding how cloud and radiation schemes perform over South Africa, representing a step forward in the state of the art. In addition to the scientific interest, the capabilities developed through this work may benefit the second largest economy of the continent. In a country where energy security is of critical relevance, the availability of useful and usable weather information is paramount to support its industry and socioeconomic growth.

KEYWORDS: Africa; Shortwave radiation; Clouds; Forecasting; Model evaluation/performance

1. Introduction

The South African Weather Service (SAWS) and the Met Office have an ongoing partnership financed by the U.K. government Newton Fund and administrated by the Weather and Climate Science for Service Partnerships (WCSSP) program. The overall goals of the WCSSP–South Africa project are to promote economic development and social welfare in South Africa, through improved weather and climate services. The work presented in this paper focuses on the development of site-specific numerical weather prediction (NWP) capabilities able to support the energy sector.

We assessed local solar (shortwave) radiation forecasts in South Africa, provided by the SAWS high-resolution NWP models, the SA models at 4- and 1.5-km spatial resolutions. Our primary aim was to investigate the skill of high-resolution SA models, to help inform future core model developments. By understanding the SA model's performance in forecasting short-term (up to 1 week ahead) location-based solar radiation, we are also contributing to South Africa's commitment to reducing greenhouse gas emissions through energy system decarbonization. As stated by the Department of Energy (2018, 2019), solar photovoltaics (PV) are expected to represent about one-third of the renewables share by 2030, which means that SAWS forecasting capabilities are of strategic interest.

We evaluated the SA model performance in predicting site-specific solar radiation. Results were compared with SAWS's ground observations across the country, as the best available representation of truth. We focused on the main contributors to forecasting errors to understand how clouds affect the predictability of surface shortwave radiation. While most of the literature on this topic has focused on northern midlatitudes, there is a lack of equivalent research in other parts of the world, namely, over sub-Saharan Africa.

Solar power technologies such as PV rely on three solar irradiance components: direct, diffuse, and global horizontal, as a baseline for the reflected component on the plane-of-array. The amount of solar energy reaching the surface at a particular location is affected by several factors, namely, clouds,

Denotes content that is immediately available upon publication as open access.

Corresponding author: Joana Mendes, joana.mendes@metoffice.gov.uk

DOI: 10.1175/JAMC-D-23-0058.1

aerosols, water vapor content, and other atmospheric gases or particles, as well as the variation of the sun angle throughout the day, seasons, and year. The fraction of solar energy passing through clouds varies with the clouds' extent, amount, and phase of condensate (Govender and Sivakumar 2019).

Improving the representation of clouds in numerical models is still one of the greatest challenges in weather forecasting (Jensen et al. 2016). Learning how different cloud regimes contribute to the radiation forecasting bias helps inform the solar resource potential and variability, which affect the efficiency of solar power production. Van Weverberg et al. (2015, 2018) have demonstrated how a differentiated analysis of model biases can lead to unambiguous interpretations of radiation errors, as compared with mean assessments. This enabled the identification of cloud regimes that contribute most to surface biases in weather and climate models over the U.S. southern Great Plains. Warm temperature biases have been shown to coincide with surface radiation biases, due to deficiencies in the surface properties, water vapor, aerosols, and most significantly clouds. Net surface shortwave radiation is systematically overestimated, with cloud (extent and radiative properties) errors dominating the radiation bias. In South Africa, Govender and Sivakumar (2019) assessed the variation of diffuse irradiance under different sky conditions in Durban. The authors identified four dominant cloud genera leading to higher variabilities in diffuse irradiance: low-level stratocumulus, midlevel altocumulus, and cirrus or spissatus high-level clouds.

In section 2, we describe the data and postprocessing methods used to analyze site-specific surface shortwave radiation and cloud forecasts against observations. The performance of both SA model resolutions and the impacts of different cloud regimes in the radiation error are outlined in section 3. Section 4 discusses the implications of these results, to help inform future NWP model developments and the optimization of applications for the renewables sector in South Africa.

2. Data and methods

a. Radiation and cloud ground-based observations

The assessment of NWP model performance relies on observational data, which can be from multiple sources, including ground-based and satellite. Although ground-based observations can have high frequencies (e.g., subhourly), they are not consistent globally, with more pronounced gaps in the Southern Hemisphere and developing countries. With a wider spatial coverage, albeit with lower temporal resolution than in situ observations, satellite remote sensing has been effective in providing surface shortwave radiation and cloud data at regional and global scales. To extract the most possible information, it is advisable to combine both ground observations and satellite data (Singh and Kruger 2017). Because the validation of satellite-based products is hindered by the limited availability of ground measurements (Singh 2016; Tazvinga et al. 2017), in this study we have chosen to focus our model analyses against site-specific observations in South Africa to further realize the value of these datasets.

Since 2015, SAWS has maintained and monitored a network of ground-based weather stations across South Africa in all its climatic zones, as per WMO (2017, 2019) guidelines. The radiometric network includes different types of instruments to measure global horizontal irradiance (GHI), direct normal irradiance (DNI), and diffuse horizontal irradiance (DIF). GHI and DIF data are collected using Kipp and Zonen CMP11 pyranometers, DNI is collected using Kipp and Zonen CHP1 pyrheliometer, and a Campbell Scientific datalogger (CR1000) is used for data acquisition. Overall, these stations provide good quality-controlled data, with a percentage of good data for all three solar radiation components ranging between 91.6% and 93.6% after Baseline Surface Radiation Network (BSRN) quality-controlled tests (Mabasa et al. 2018).

In all radiometric stations, solar radiation data is acquired with a sampling rate of 5 s. To guarantee that hourly time stamps correspond to the respective hour of the day, we process the observation data in four steps, as adopted by Mabasa et al. (2019, 2020, 2021): 1) the mean, maximum, minimum, and standard deviation for GHI, DIF, and DNI are collected for each minute; 2) BSRN observation quality checks are performed to remove outliers, as per WMO (2013) and Long and Dutton (2010); 3) the minute data are averaged to 15 min; and 4) hourly averages are calculated by aggregating four consecutive 15-min averages.

To enable a direct comparison between the hourly averaged radiation observations and the (hourly) instantaneous radiation forecasts, the observations are mapped onto instantaneous values valid at the corresponding time stamp. This was achieved in four steps (illustrated in Fig. A1 in appendix A): 1) multiply DNI by the cosine of the zenith solar angle to get direct horizontal irradiance (DHI); 2) divide the radiation observations by the top-of-atmosphere (TOA) radiation at the time to obtain a transparency factor; 3) take the transparencies, valid at the midpoint of each hour, and interpolate to the hour; and 4) multiply by the TOA radiation valid at the hour to obtain values in watts per meter squared. The times at which cloud observations are valid are simply converted from South African standard time (SAST, i.e., UTC + 2 h) to UTC. Cloud fraction values are obtained by dividing the total amount in okta by eight; for example, 1 and 7 okta have observed cloud fraction values of 0.125 and 0.875, respectively.

In addition to solar radiation, SAWS takes observations of clouds manually (by an observer) 3 times per day at 0800, 1400, and 2000 SAST, in 12 different locations mostly corresponding to where the solar radiation stations are located. Clouds are measured according to international air navigation regulations (WMO 2018), which means in some cases the total cloud cover may have more than 8 okta when adding together low, medium, and high cloud cover components. Manual synoptic observations of total cloud amount are instantaneous and hemispheric, providing at one point in time a three-dimensional volume average of all clouds visible out to the visible horizon, representative of an area between 10 and 100 km (WMO 2017). Automated cloud observations are, on the other hand, a time aggregate of cloud passing downwind through advection, and hence not hemispheric.

It is often assumed that all errors are from the model, hence ignoring any uncertainties in the observations. Although the same instruments are used throughout the SAWS radiometric network and the overall quality-control performance is up to standards, it is important to point out that these stations might be at different stages of the maintenance cycle, and so differences in sensitivity and calibration between sites may occur. When validating NWP forecasts against observational data, it is also important to note that gridscale modeling may not accurately represent an area of actual model spatial resolution (or less) because of the variability of weather parameters at those scales.

Additionally, differences in cloud observations may result from varying manual observation practices at different locations. Synoptic observations represent an area of up to 100 km around the station; however, they may not be fully representative of the small scale, as observed by Mittermaier (2012). The author points out that different types of observation may impact model forecast errors with reverse signals, as manned observations of total cloud amount tend to report fewer events of 0 and 8 okta. An underestimation of clear sky and overcast could be associated with a restricted hemispheric view, the difficulty to measure clouds during nighttime, or even a result of inconsistencies between different observers in different locations. It can also be due to hedging for reports of cloud cover to the nearest okta. For example, if the cloud cover is 0.4 okta, it may get rounded up to 1 okta, when it should be rounded down to 0 okta, because the human observer reckons there is some cloud in the sky; similarly, this can also happen for the 8-okta end. This means that observations may in fact have an impact on the magnitude of forecast biases and skill scores.

b. *MetUM and SA NWP models*

SAWS runs a suite of operational NWPs named the South Africa (SA) model, underpinned by the Met Office Unified Model (MetUM). The MetUM is a seamless convection-permitting numerical model, which means it can predict across a range of spatial and temporal scales with a consistent dynamical core and parameterization schemes. It uses a global driving model and regional models that can be applied anywhere in the world. Examples of the MetUM NWP at kilometer-scale can be found in Keat et al. (2019), Van Weverberg and Morcrette (2022), and Webster et al. (2008).

Although kilometer-scale is more commonly used in limited-area NWP, convection-permitting climate models, such as the MetUM, have been investigated by Schär et al. (2020) and Kendon et al. (2023). Extending a highly resolving capability to time scales farther ahead is increasingly valuable for local solar power applications under a changing climate. While empirical simulations involve a much lower computational cost than traditional numerical modeling, the coarser resolution at which many empirical models operate may constrain their ability to predict at the local scale. Jiang et al. (2015) and Zhang et al. (2014) present linear models that skillfully estimate solar radiation based on past data relationships; however, their predictability is limited to short-term horizons.

In this study, we focus on the site-specific assessment of high-resolution numerical weather predictions. The global configuration of the MetUM has a grid resolution of around 10 km, which then drives the higher-resolution regional NWPs over South Africa at 4 km (SA4) and 1.5 km (SA1.5) (Stein et al. 2019). Increased spatial resolution enables a better representation of convective phenomena (Clark et al. 2016; Lean et al. 2008). We have analyzed all configurations: SA4 initialized at 0000 and 1200 with a forecast range of 72 h, and at 0600 and 1800 out to 48 h ahead, and SA1.5 initialized at 0000, 0600, 1200, and 1800, with a forecast range of 36 h.

Instantaneous hourly forecasts of DHI and DIF irradiance, valid for each forecast lead time are produced; total downward surface shortwave radiation (GHI) is derived as the sum of DHI and DIF components. Direct model outputs of separate direct and diffuse instantaneous forecasts use a correction, translating fluxes to a mean over the current model time step. The SA model radiation scheme features a delta-Eddington approximation for a more accurate total flux. However, this leads to scattering in the forward direction being ignored, thus enhancing the direct flux artificially, which is often larger than pyrheliometer observations. As for the diffuse component, the model includes a fraction of incident radiation from the direction of the sun, which would be excluded from the value measured by a diffuse pyranometer using a shadow band.

The total cloud amount at each grid box is also predicted and analyzed. In the case of instantaneous cloud forecasts, these represent an area average defined by the grid box. Effectively, they correspond to a time average dependent on the advection speed, which is offset relative to observations. The SA4 and SA1.5 use the same physics schemes and parameterizations as the 4-km European and 1.5-km U.K. versions of the MetUM, respectively. The global driving configuration uses Wilson et al.'s (2008) prognostic cloud fraction and prognostic condensate scheme (PC2), with a fixed profile for critical relative humidity, as per Smith (1990). The radiative transfer scheme is based on the Suite of Community Radiative Transfer Codes Based on Edwards and Slingo (SOCRATES; Edwards and Slingo 1996; Manners et al. 2018) with a global atmosphere 3.1 (GA3.1) configuration (Walters et al. 2011), whereby solar radiation is composed of six shortwave bands and thermal radiation in nine longwave bands (Bush et al. 2020). According to Van Weverberg et al. (2021), current MetUM cloud schemes tend not to be binary enough, underpredicting clear sky or overcast and overestimating partly cloudy events, while not scaling well with resolution.

NWP models are designed to capture the regional to large-scale meteorological flow. However, this might not be accurate enough on the local scale, where orography and land use play an important role near the ground. NWP postprocessing addresses inconsistencies in the grid and location-based forecasts, to reduce errors. SAWS has been running a postprocessing system operationally since 2017, generating site-specific SA4 and SA1.5 forecasts adjusted to local features. Corrections of surface diagnostics take into consideration a higher-resolution representation of the terrain and land use. Additionally, site selection from the gridded data applies nearest neighbor interpolation, whereby the selected grid point is closest to the observation station with similar altitude and land–sea mask

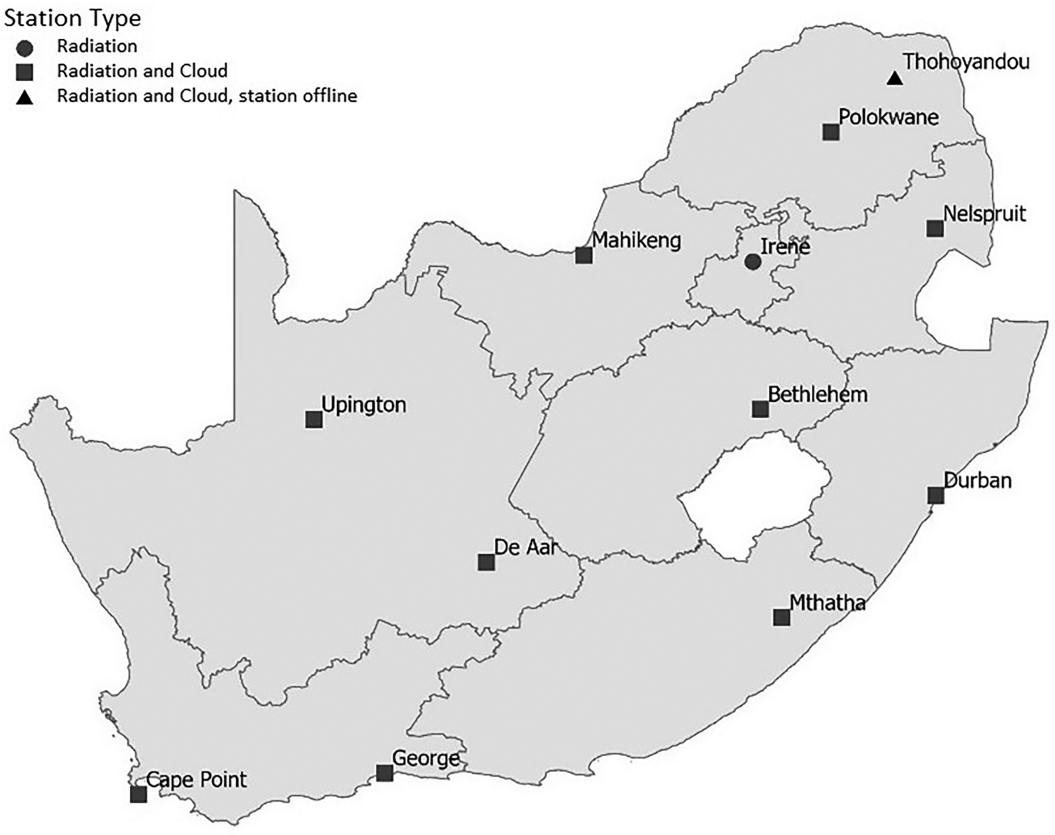

FIG. 1. Geographic distribution of SAWS radiometric stations.

characteristics. Above, we described how hourly averaged radiation observations and instantaneous cloud observations have been processed, allowing the comparison with instantaneous forecasts for the nearest model grid point.

c. *Methodology*

Model verification relies on the availability of in situ observations and site-specific forecasts. In this study, we have used observations taken across South Africa for the period between April 2017 and August 2018, as illustrated in Fig. 1.

We compared model performance for SA1.5 and SA4 forecasts of surface shortwave radiation (total, direct and diffuse) and clouds (total amount). Figure 2 presents a flow diagram of the methodology adopted.

The following evaluation metrics, which are of interest for energy applications, were calculated: mean bias error (MBE), mean absolute error (MAE), and root-mean-square error (RMSE), along with the respective normalized mean errors (nMBE, nMAE, and nRMSE) against a measure of spread, in this case, the difference between maximum and minimum observations. The standard deviation error (SDE), coefficient of determination R^2, and percentiles of the mean predicted error have also been calculated for the lower (P5), upper (P95), and median (P50). Despite providing an indication of the quality of a forecasting model, single metrics or a limited set of measures may not capture the whole complexity and dimensionality of model verification. To differentiate spatial and temporal sources of error, a grouped statistical analysis was done for site, model run, forecast lead time, time of day, and month of the year.

A separate analysis has also been done for daylight hours only and all day to understand how night affects day results when combined. Different times of day and season can affect the magnitude of surface shortwave radiation errors, particularly around midday and in the summer. To discern model errors from the natural variability in solar radiation, we calculated the errors relative to the TOA radiation (for the corresponding locations and time of the year). This transformation allows to isolate atmospheric dispersion from aerosols, providing the forecasting error in the fraction of shortwave radiation reaching the ground.

Additionally, a cloud-dependent assessment has been adopted to infer the role of clouds in solar radiation errors. In the presence of clouds, the assumption is that errors in surface shortwave radiation are more likely due to errors in cloud prediction. When the sky is clear, we expect errors to be mostly attributed to aerosols and radiative transfer through gases in the atmosphere. In other words, for correctly predicted clear sky, there is no cloud error. For partial cloud or incorrectly predicted cloud, both cloud and aerosol errors are combined. To better understand the contribution of different cloud regimes to the error distribution of surface shortwave radiation, we classified cloud amount according to the

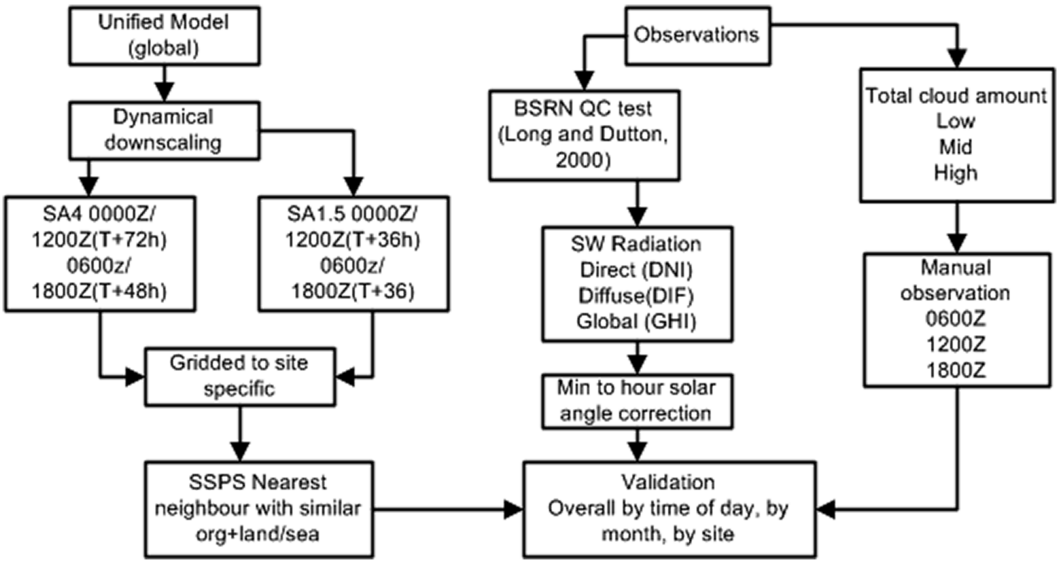

FIG. 2. Flow diagram of model analysis.

frequency of cloud fraction and the respective mean radiation value for each regime.

3. Results

a. Radiation

Surface shortwave radiation analyses used ground-based observations, as shown in Fig. 1, and SA1.5 and SA4 site-specific forecasts, as described in section 2b. Results are presented for model runs initialized at 0000 UTC, as no substantial differences were found for other initializations.

The primary model performance metrics are the MBE corresponding to positive/negative systematic errors (i.e., over/underprediction); MAE, measuring the mean correspondence between individual pairs of forecasts and observations; and the RMSE, which quantifies the combined systematic and random errors. The closer to 0 W m^{-2} these errors are, the more unbiased the forecast is. Additionally, we have assessed surface shortwave radiation forecasts using the normalized mean errors (nMBE, nMAE, and nRMSE) as percentage metrics to differentiate between maxima/minima biases or variability; the SDE, measuring the uncertainty of biases around the mean (i.e., square root of the variance); and the coefficient of determination (R^2) indicating the proportion of variance explained by a linear regression model (1 corresponds to a perfect score). The 5th (P5), 50th (P50), and 95th (P95) percentiles were also calculated to provide an indication of the spread of errors against a normal distribution.

Tables 1 and 2 show the overall forecasting error results, respectively, for the SA4 and SA1.5 models. Across all stations and the whole evaluation period, SA4 tends to overestimate GHI and DHI, whereas DIF is slightly underpredicted, as shown by the MBE. The largest net forecasting errors, both systematic and random, occur for the direct component of radiation, as seen by the MAE and RMSE values. Normalized mean errors, representing the overall proportion of errors relative to radiation maxima are consistent with these results. The model artifacts mentioned in section 2b can partially explain these results, namely, the artificial enhancement of DHI and the derivation of GHI. Differences between direct, diffuse, and total radiation biases, as well as their relation to cloud errors, are further discussed in the following subsections.

Results are similar for the SA1.5 model, albeit slightly more biased overall. The higher-resolution model presents reversed signals of systematic biases, with a positive MBE for the diffuse component and negative bias for the direct radiation and global radiation. Although using the same parameterization schemes, neither of the SA models incorporate data assimilation or additional convective-scale information. This could lead to differences between the models' representations at grid and subgrid scales and the actual weather variability. However, the effects of spatial resolution in the SA model performance are still unclear and would require further investigation.

Geographically (see Fig. A2 in appendix A), errors agree with the overall results, with no clear distinction between

TABLE 1. SA4 surface shortwave radiation errors.

Radiation (W m^{-2})	MBE	nMBE (%)	MAE	nMAE (%)	RMSE	nRMSE (%)	R^2	SDE	P5	P50	P95
GHI	6.7	0.6	40.7	3.4	106.4	8.9	0.9	106.1	−94.9	0.0	137.7
DHI	19.4	1.7	51.9	4.6	126.5	11.2	0.7	125.0	−99.6	0.0	74.3
DIF	−0.7	−0.1	28.3	2.8	63.0	6.3	0.6	63.0	−81.8	0.0	238.9

TABLE 2. SA1.5 surface shortwave radiation errors.

Radiation (W m^{-2})	MBE	nMBE (%)	MAE	nMAE (%)	RMSE	nRMSE (%)	R^2	SDE	P5	P50	P95
GHI	−6.5	−0.5	50.2	4.2	121.9	10.2	0.9	121.7	−180.6	0.0	125.5
DHI	−6.3	−0.6	63.3	5.6	145.3	12.9	0.7	145.1	−90.7	0.0	134.4
DIF	9.6	1.0	35.8	3.6	75.5	7.5	0.4	74.9	−231.5	0.0	189.8

different climatic regions in South Africa or coastal/inland locations. This means that local differences can be attributed to the variability between radiometric stations, rather than due to the model's ability to represent local features, such as orography or sea breezes contributing to atmospheric dispersion.

Radiation results aggregated by hour and by month (see Figs. A3 and A4, respectively, in appendix A) show strong diurnal cycles for all radiation components, with errors peaking around the middle of the day. Although the RMSE (and MAE) follow a seasonal trend, no seasonal pattern is seen for the mean bias. Furthermore, there is an increase in the spread of observations (and forecasts) in the middle of the day (and summer). Daytime only radiation analysis has shown that excluding the nighttime period increases mean errors, which is consistent with a slight masking of daytime skill when compared with (perfect) nighttime forecasts. The normalized mean errors provide useful information about the predictability of diurnal and seasonal cycles. These errors are constant throughout the day and year, meaning that error maxima are likely due to the radiation peaking in the middle of the day and summer, rather than a lower model skill at those times. In addition, the surface shortwave radiation was scaled against the TOA radiation, to remove the influence of the TOA (results are displayed in Tables A1 and A2 for SA4 and SA1.5, respectively). Scaled radiation errors do not follow a diurnal pattern (see Fig. A5), suggesting that atmospheric dispersion might be contributing to the maxima of radiation errors.

For the remaining metrics presented in Tables 1 and 2, the coefficient of determination in both models is closest to 1 for GHI, indicating a better linear fit between observations and forecasts for the global component, when compared with direct and diffuse radiations. However, the asymmetry between lower and higher percentiles against P50 suggests that the variance of the errors is not constant across the distribution. A lack of homogeneity in the variance means the error distribution does not comply with the principle of homoscedasticity, upon which an ordinary least squares approach is based. Hence, the median, which is virtually 0 W m^{-2} across all radiation components, is a better indicator of the error's central tendency than the mean; also, the lowest/highest percentiles provide a more meaningful estimation of the spread than does 2 times the standard deviation.

The relative deviation from a normal distribution is provided by the skewness of the errors. The SA4 model is left-skewed for GHI and DHI, which means that it tails off to the left and the mass of the distribution of the error is concentrated on the higher percentiles. The diffuse component is, on the other hand, right skewed indicating that a greater proportion of the DIF errors are concentrated on the lower radiation values. Similar results were obtained for the SA1.5, suggesting that both model resolutions tend to misrepresent more of the smaller diffuse radiation and more of the larger direct and global radiation. Differences in skewness between radiation components can be explained by the optical properties of clouds. While cloud scattering in the forward direction enhances the direct flux, the diffuse component reacts to the presence of cloud in the opposite way.

b. *Cloud*

Assuming the correct representation of radiative transfer in the atmosphere and a correct profile of aerosols and humidity, we expect an increase in cloud cover to result in the reduction of solar radiation at the surface. On the other hand, the misrepresentation of cloud in NWP modeling is likely the main driver of surface shortwave radiation forecasting error. We have analyzed how the SA models perform in predicting total cloud amount and frequency of occurrence by comparing with available observations at 0600, 1200, and 1800 UTC.

For verification, cloud regimes are classified based on the mean cloud fraction (AVG), corresponding to the product between the frequency of cloud occurrence and mean amount when present, as in Morcrette et al. (2012). Cloud amount has been translated into a fraction for each categorical level, as shown in Table 3, enabling error differentiation for apparently

TABLE 3. Cloud regime classification based on observed and model forecast cloud fraction.

Classification	Cloud cover (okta)	Obs cloud fraction	Model cloud fraction range
Clear	0	0	[0]
Few	1	0.125	(0, 0.1875)
Few	2	0.25	[0.1875, 0.3125)
Scattered	3	0.375	[0.3125, 0.4375)
Scattered	4	0.5	[0.4375, 0.5625)
Broken	5	0.625	[0.5625, 0.6875)
Broken	6	0.75	[0.6875, 0.8125)
Broken	7	0.875	[0.8125, 1)
Overcast	8	1	[1]

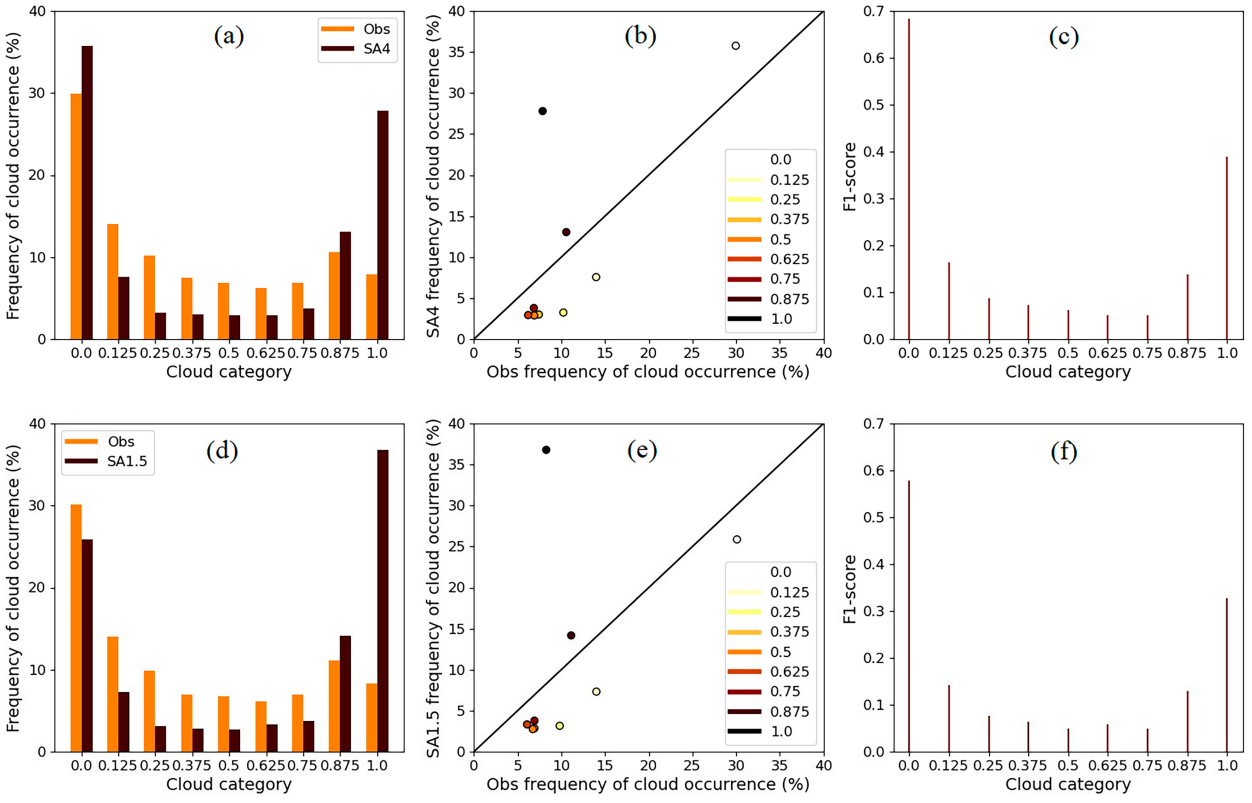

FIG. 3. Distribution analysis of total cloud for each cloud regime, showing (a),(d) the frequency of observed and predicted cloud occurrence per category; (b),(e) the corresponding quantile–quantile plots; and (c),(f) the F1 score per category for (top) SA4 and (bottom) SA5.

"good"/"bad" AVG. For example, if at a given location the AVG cloud amount is 4 okta (or 0.5 cloud fraction category), and this is because the cloud cover is 4 okta for the whole hour, then a model producing 0 okta half the time and 8 okta the other half the time would appear to be a good forecast on average. However, a different model predicting 3 okta all the time would seem to have a larger AVG error, although it is a better forecast; this would be reflected in the errors of frequency of occurrence and mean cloud when present.

Figure 3 illustrates the distributions of total cloud, reflecting the frequency of events for each cloud category (as per cloud fractions indicated in Table 3). Figures 3a and 3d present the histograms of observed and forecast cloud occurrence, respectively, for the SA4 and SA1.5. Contrary to what was found by Van Weverberg et al. (2021), the SA models are mostly confined to the tails, reflecting the binary prevalence of clear-sky and overcast events. Figures 3b and 3e show the corresponding quantile–quantile plot, where the nine quantiles equate to the partitions of cloud regimes. The quantiles do not follow a linear pattern, suggesting the data are not normally distributed. The frequency of other cloud categories is slightly underestimated, except the 0.875 cloud regime, which is marginally overpredicted. Overcast regimes are strong outliers, where the greatest proportion of the errors is concentrated, leading to an overall positive bias. Although an increase in horizontal resolution does not seem to significantly improve the spread of distributions, it would be premature to conclude that the higher-resolution model has less skill in predicting cloud.

Figures 3c and 3f show the F1 scores for each cloud category. Given the imbalance in the cloud distributions, we have used the F1 score as an indicator to reduce both false positives and false negatives of cloud events for each regime. The F1 score corresponds to the harmonic mean of precision and recall, measuring both the predicted positive rate and true positive rate. Ranging between 0 and 1, where 1 is a perfect score, the F1 score plots show that the SA models are more successful predicting clear-sky events at the right time, followed by overcast. The models perform less well at predicting when the remaining cloud categories occur.

Clouds are discrete by nature; we are comparing an instantaneous gridbox forecast of total cloud amount (derived from model profiles using maximum-random overlap) averaged over a 4 km × 4 km or 1.5 km × 1.5 km area with instantaneous observations across a large-hemisphere region (of 10–100-km radius). This means that cloud features may not be in the right place at the right time, which could lead to a double penalty of errors in space and time. Despite limitations in the availability of manual cloud observations in this study, automated measurements should not be assumed to be better, as pointed out by Mittermaier (2012). Furthermore, the difference between cloud cover recorded by a human observer and

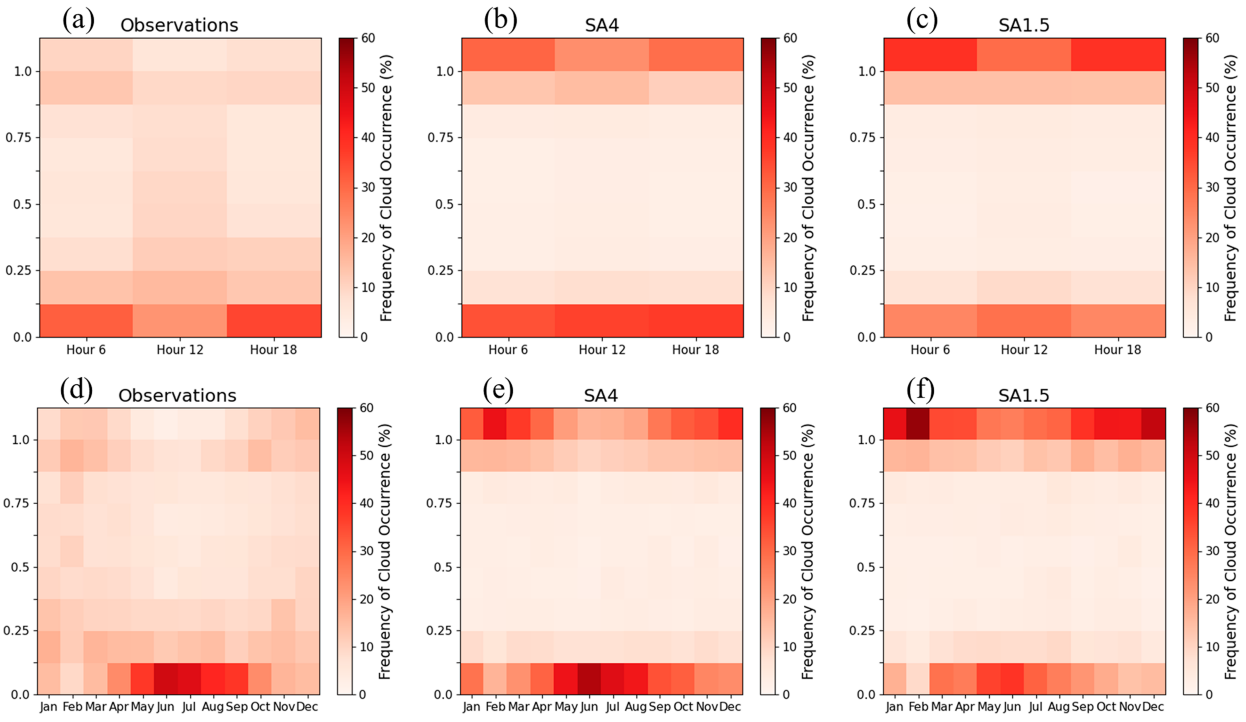

FIG. 4. Frequency of total cloud occurrence for (left) observations, (center) SA4, and (right) SA1.5 (top) at 0600, 1200, and 1800 UTC and (bottom) per month.

those inferred from radiometer observations are discussed by Long et al. (2006). Here it would be important to ascertain differences between an observer hedging away from the boundaries (clear sky/overcast events) in South Africa in comparison with other studied parts of the world.

Across observation locations in South Africa, the frequency of cloud occurrence differs for low levels (0–3 km AGL), midlevels (3–6 km AGL), and high levels (6–20 km AGL) (see Fig. B1). Low-level clouds are seen more often in the morning, high clouds occur more commonly in the middle of the day, and midlevel clouds in the evening. Cloud amount when present (i.e., for all regimes except clear sky) is larger in the morning and smaller in the evening; however, it is not possible to ascertain cloud continuity between levels. Fewer clear-sky events have been observed in the afternoon than at other times of the day. Low-level clouds are also the most frequent throughout the year, with fewer mid- and high-level clouds observed in the winter, suggesting the prevalence of stratus and cumulus clouds during those months.

The models have a consistent performance across South Africa (see Fig. B2 in appendix B), and no differences were observed between inland and coastal atmospheric dispersion (which drives cloud genera). Further investigation into cloud forecasting error attribution has been carried out for different times of the day and year, as shown in Fig. 4.

Figure 4a presents the frequency of occurrence of observed total cloud in the morning, middle of the day, and evening for each category. Both SA models (Figs. 4b,c) predict the overall frequency of clear-sky events relatively well, with a few differences: SA4 overpredicts the occurrence of cloud-free events in the afternoon, whereas SA1.5 slightly underpredicts these events in the morning and overpredicts them in the afternoon. For other cloud regimes, SA1.5 and SA4 consistently overpredict overcast events, predominantly forecasting such categories to the detriment of other cloud categories. Although clear-sky events are observed most often, other cloud regimes are seen throughout the day, particularly in the afternoon. Hence, larger cloud frequency biases found at 1200 UTC could be a result of the NWP model not capturing some of the cloudiness associated with heat-induced convection, although this would have to be clarified.

An interesting observation in South Africa is that there are more clear-sky events in the winter and more cloud events in the summer (see Fig. 4d), as opposed to other countries in the Northern Hemisphere (Mittermaier 2012; Morcrette et al. 2012; Van Weverberg et al. 2015, 2018). Throughout the year, cloud results are consistent with the above. As shown in Figs. 4e and 4f both SA models present a binary prevalence toward extreme cloud categories, overpredicting overcast events and underestimating the frequency of occurrence of scattered and broken cloud ranges. SA4 is more skillful at predicting the clear skies that occur more frequently during the winter months. The models are not able to capture, in either season, enough of the relative abundance of broken or stratiform clouds in comparison with cloud-free or overcast skies.

c. *Cloud-dependent radiation analysis*

A cloud-dependent radiation analysis has been performed to further disentangle the effects of different cloud regimes

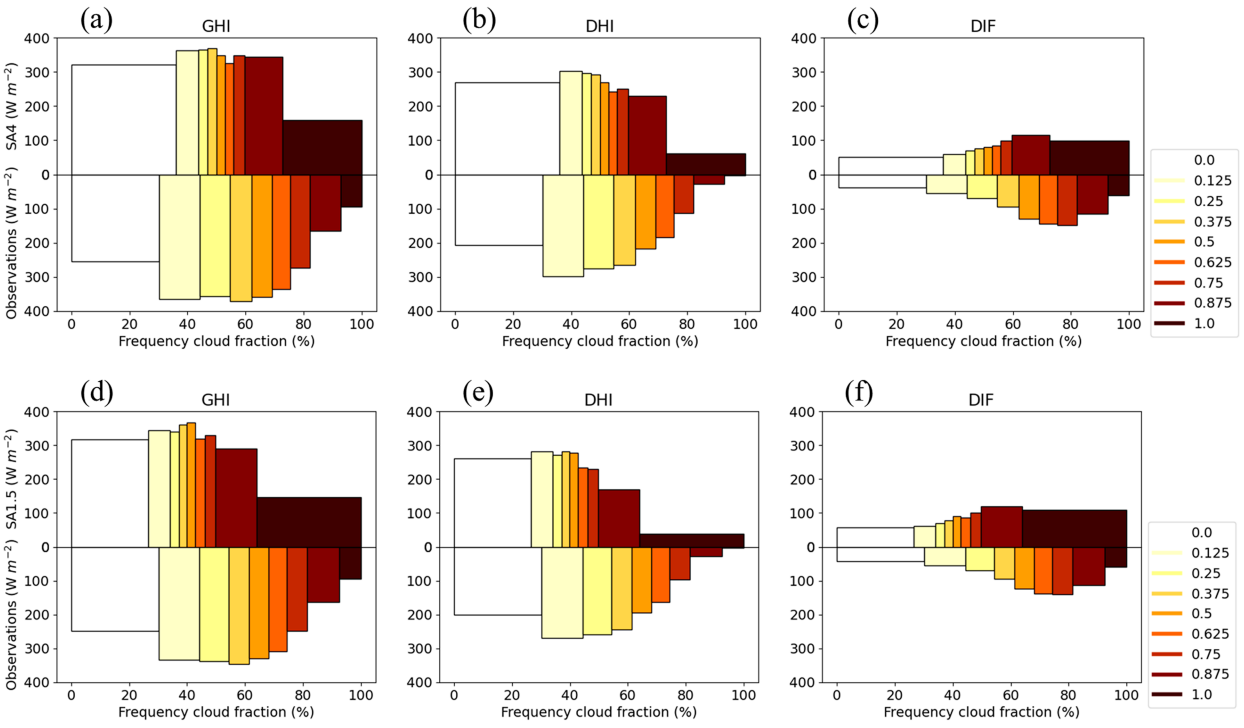

FIG. 5. Frequency of occurrence for each cloud fraction category (width) and their respective impact on the mean surface shortwave radiation (height), comparing forecasts (top half of each panel) with observations (bottom half of each panel) for all radiation components for (a) GHI SA4, (b) DHI SA4, (c) DIF SA4, (d) GHI SA1.5, (e) DHI SA1.5, and (f) DIF SA1.5.

in the SA model's surface shortwave radiation forecast error. This is based on the categorization of total cloud fraction between 0 and 1 (as unitary fraction of okta), to identify which cloud ranges contribute more to radiation errors, or whether these errors are due to the model misrepresentation of different cloud regimes. Results are shown for the model initialized at 0000 UTC, as no major differences were found from the normalized analysis and other model runs. Note that only cloud-free (0) and fully overcast (1) events have been reported for the minimum and maximum total cloud fractions; plus, cloud observations are exclusively available at 0600, 1200, and 1800 UTC, which limits the concurrent validation periods and constrains farther extrapolations in time.

Figure 5 presents the frequency of occurrence for each cloud fraction category (width) and their respective mean surface shortwave radiation (height), comparing both SA4 and SA1.5 models. Forecasts (top half of figure) are laid over observations (bottom half of figure) for each radiation component, illustrating how often each cloud range occurs and how it impacts radiation. For a given cloud category (each represented by a different color box), compare the width (for the frequency of occurrence of that cloud regime) and the height (for the mean radiation of that category). A perfect forecast corresponds to a symmetric reflection, which means that a certain cloud category is biased if the model cannot replicate its frequency well enough (smaller/larger widths) and/or if it cannot accurately represent the radiation properties associated with that regime (smaller/larger heights).

To help interpret the impact of each cloud fraction category on the surface shortwave radiation, we have included the numerical results of Fig. 5 in appendix A (Tables A3 and A4 for SA4, and Tables A5 and A6 for SA1.5). Taken across all cloud regimes, the overall radiation bias is positive (i.e., predicting too much of it); however, counterintuitively this happens alongside an overestimated frequency of the overcast cloud regime. For all radiation components, both models overestimate the frequencies of 7–8 okta (0.8125–1.0) events, predominantly the fully overcast category, which can represent almost 30%–40% of the frequency of cloud occurrence that was forecast. Not only these cloud regimes are predicted too often, but also the expected mean amount of radiation is overestimated, particularly in the summer. The relative abundance of other cloud regimes largely contributes to the radiation errors. For example, the frequencies of 1–6 okta (0.125–0.75) cloud events are underpredicted, with GHI and DHI positively biased but a negative bias for DIF; from these, the 0.125 cloud category agrees better with the observations. The frequency of clear-sky events is relatively well predicted by both SA model resolutions. Overall, the mean radiation magnitude tends to be slightly overestimated, albeit less so than in subsequent cloud categories, namely, for the global and direct components. This may seem counterintuitive, because one would expect more shortwave radiation to reach the surface when no clouds are present; however, surface radiation maxima may not be more frequent under cloud-free regimes.

Small differences were seen between model resolutions, and these are further discussed in section 4. Earlier in the day, SA4 predicts well the frequency of clear-sky while SA1.5 slightly underpredicts these; in the afternoon both models overpredict the occurrence of cloud-free events and overestimate mean radiation. Seasonally, the variation of clear-sky events is much more pronounced than for scattered/broken and overcast cloud regimes, peaking in winter, although with opposite bias signals between the SA1.5 and SA4.

As a caveat reminder, the results shown in Fig. 5 only consider 3 times of the day (at which cloud observations are available). Also note that cloud-free events tend to be more frequent in the morning and evening when the radiation is lowest (see Fig. B1 in appendix B). In addition to that, partly cloudy regimes may intensify solar radiation, particularly for convective types of cloud that are not obstructing the sun's disk (Matuszko 2012). This suggests that aerosols and radiative transfer through other gases could be contributing to an overall positive radiation bias under clear-sky regimes.

4. Discussion

The SA models have skill in predicting surface shortwave radiation, with zero median bias across South Africa. The median was used as a better representation of the overall error's central tendency for all sky (including clear-sky and cloudy regimes), and results are consistent geographically. Overall biases in total, direct and diffuse radiation follow a diurnal cycle peaking around midday, which is attributed to the degradation of forecasting skill at that time of day (as demonstrated by the scaled results). Errors are also higher in the summer (and lower in the winter) due to the variation in mean solar radiation throughout the year. These results agree with the analysis of Singh and Kruger (2017), who investigated seasonal trends over a 60-yr period, using sunshine duration observations from SAWS radiometric network and the Surface Solar Radiation dataset (SARAH) produced from the EUMETSAT Climate Monitoring Satellite Application Facility (CM SAF).

Diffuse radiation errors are, in general, the lowest of all components. While it is overpredicted by the SA1.5 and underpredicted by the SA4, the direct component is reversely biased. To understand how the relative predictability of different non/cloud regimes impact the SA models' ability to forecast solar radiation, we performed a baseline cloud analysis, in terms of the mean amount (overall, including clear sky), as well as the frequency of cloud occurrence and amount when present (excluding cloud-free events); clear-sky regimes have also been analyzed separately.

Cloud-free events dominate the observations (available at 3 times of the day only), and the frequency of occurrence when cloud is present decreases with an increase in the amount of cloud (up to 6 okta). Both SA model resolutions mainly predict clear-sky and overcast regimes, leading to a (small) positive bias in the mean cloud amount. Our results are different from those of Van Weverberg et al. (2015) over Oklahoma, where partly cloudy categories were predicted too often against not enough occurrences of (near) cloud-free and (near) fully cloudy events. This is due to differences in the choice of convection and cloud parameterization schemes used in the MetUM global model of that study versus in the regional SA models used here.

In general, manual cloud observations tend to underreport clear skies and overcast events (Mittermaier 2012). However, our analysis has shown that the overprediction of near overcast and overcast events masks the underprediction of partly cloudy regimes. In strict terms, we are comparing the instantaneous gridbox forecast average of total cloud amount over a 4 km $\times$ 4 km or 1.5 km $\times$ 1.5 km region with instantaneous observations over a large-hemisphere region. Because clouds are discrete, their modeled features may not be in the right place at the right time, which means that cloud errors can be double penalized in space and time.

The subgrid representation of temperature and moisture variability determines how much of the grid box is assumed to be over saturation when the gridbox mean value is below saturation, and thus the amount of cloud expected to form. For larger grid boxes, less of the thermodynamic variability is resolved by the model, while more of it requires parameterization. This has further implications for the amounts of radiation passing through the grid box as well.

Van Weverberg et al. (2016) argue that the critical relative humidity is sensitive to the horizontal and vertical model resolutions, impacting the performance of cloud forecasts. The authors found that representing subgrid humidity fluctuations is relevant for determining cloud cover, even for models running with kilometer-scale grid lengths. By adjusting the MetUM cloud scheme from a constant critical relative humidity to a turbulence-based profile, they found that cloud cover predictions were improved, particularly in terms of reducing the sensitivity of the cloud cover forecast to the choice of resolution used in the model.

These findings were used as a baseline for our cloud-dependent radiation analyses, to identify whether the surface shortwave radiation error is mostly due to specific cloud regimes not being correctly predicted, and/or a result of the misrepresentation of the relative abundance across cloud categories. This was based on cloud classification of nonzero events and respective mean solar radiation. For both SA model resolutions, the cloudiest ranges (7–8 okta) represent about half the frequencies of occurrence (many more than observed), leading to a positive bias in solar radiation under those regimes. Although this could be attributed to cloud properties, such as liquid water content, not being correctly represented in the model, thus increasing the amount of radiation transmitted through the cloud, the large underprediction of partly cloudy events (1–6 okta) could have a bigger impact on radiation errors. The imbalance between cloud regime frequencies and amount when present, combined with a positive/negative mean bias for scattered or broken cloud regimes, results in opposite bias signals between direct and diffuse radiation components.

Mean radiation under clear skies, on the other hand, tends to be slightly overestimated, despite the frequency of cloud-free events being relatively well predicted. This positive bias may be associated with the underrepresentation of aerosols in

the model and the consequent decrease of radiative transfer through (these and other) gases. In fact, Singh (2016) and Singh and Kruger (2017) have found a decline in surface shortwave radiation in South Africa between the 1980s and 2000s, likely as a result of the country's industrial growth and higher concentrations of pollutant particles in the atmosphere, such as aerosols, albeit with seasonal variations.

5. Conclusions

This paper presents the first assessment of the South African Weather Service's high-resolution numerical weather predictions for site-specific surface shortwave radiation in South Africa. The SA models are underpinned by the Met Office's MetUM NWP (used worldwide), producing skillful forecasts at 1.5- and 4-km spatial resolutions. Overall, solar radiation is predicted with zero median error in all radiation components, and the models exhibit consistent performance across the country and seasonally. These results provide additional confidence in the quality of day-to-week-ahead location-based radiation forecasts, which can better support the growth of renewables in South Africa and potentially contribute to the reduction of greenhouse gas emissions in the country.

In addition to the mean assessments of surface shortwave radiation forecasts against countrywide observations at different times of day and year, we have also investigated sources of error in the SA models contributing to each component of solar radiation, namely, the role that clouds play. While cloud cover tends to be overpredicted, this does not necessarily correspond to an underestimation of solar radiation. We have seen that the relationship between cloud and radiation errors is imbalanced, as the occurrence of overcast regimes is overpredicted with a positive mean radiation bias, and the relative occurrence of partly cloudy regimes is underpredicted by the SA models, with mixed radiation biases. These differences have a great impact in the error attribution of surface shortwave radiation, namely, in the (smaller) overall bias of the diffuse component.

The combined cloud and radiation analyses in South Africa have highlighted challenges in the SA model configurations and the underlying MetUM. Sensitivity studies on parameterizations, cloud and radiative transfer schemes could inform future core model improvements. Further investigation is needed to ascertain the impacts of spatial resolution and site-specific postprocessing in the SA models, as finer scales have not shown improvements in the predictability of surface shortwave radiation. In addition, to help to clarify radiation error attribution, the relative impacts of other sources of forecast error, such as atmospheric pollutants and water vapor content, would also require more attention in future studies in South Africa.

Acknowledgments. This work and its contributors were funded by the Met Office Weather and Climate Science for Service Partnership (WCSSP) South Africa project, which is supported by the Department for Science, Innovation & Technology (DSIT). The authors also acknowledge support from the National Research Foundation of South Africa.

Data availability statement. All data created or used in this study are available upon request to the South African Weather Service.

APPENDIX A

Radiation Errors (Per Location, by Hour and Month, and Scaled)

Figure A1 illustrates the methodology applied to transform hourly averaged radiation data onto (hourly) instantaneous values. Surface shortwave radiation observations (on the half-hour) are represented by red crosses in Fig. A1a. These are transformed into a transparency factor, by dividing by the incoming TOA shortwave radiation (represented by black crosses in Fig. A1a), to produce the cyan crosses in Fig. A1b. The transparency on the half hour (cyan crosses) is then linearly interpolated to transparency on the hour (blue circles in Fig. A1c). The surface shortwave radiation on the hour (magenta circles in Fig. A1d) is found by multiplying the transparency on the hour (blue circles) by the incoming TOA shortwave radiation on the hour (black circles in Fig. A1d). Note that this yields a different result than simply interpolating the red crosses to the hour (green circles).

Figure A2 shows the surface shortwave radiation RMSE at each radiometric station, comparing SA4 and SA1.5 forecasts for the three radiation components. No geographical patterns in the errors are observed. Results are consistent with the overall errors presented in Tables 1 and 2.

Figures A3 and A4 illustrate the surface shortwave radiation errors aggregated by hour of the day and by month, respectively, comparing SA4 and SA1.5 forecasts for the three radiation components. Errors exhibit a diurnal cycle with larger magnitudes around the middle of the day. Although the RMSE (and MAE) exhibit a seasonal pattern, this is not seen for the mean bias. Signals of the hourly and monthly mean biases are consistent with the overall errors presented in Tables 1 and 2.

Tables A1 (SA4) and Table A2 (SA1.5) present the error statistics results for the surface shortwave radiation, scaled by the TOA radiation, for the three radiation components. The overall mean biases are virtually zero.

Figure A5 shows the mean bias of the scaled surface shortwave radiation aggregated by hour. There is no evident diurnal cycle, with a slight increase in the hours preceding nighttime.

Tables A3–A6 show the numerical results displayed in Fig. 5. For each cloud fraction, the frequency of cloud occurrence corresponds to the width of the box (in percentage); the mean GHI, DHI, and DIF correspond to the height of the box (in watts per meter squared) for that category; the impact of cloud on the radiation component is represented by the area of the box (in watts per meter squared).

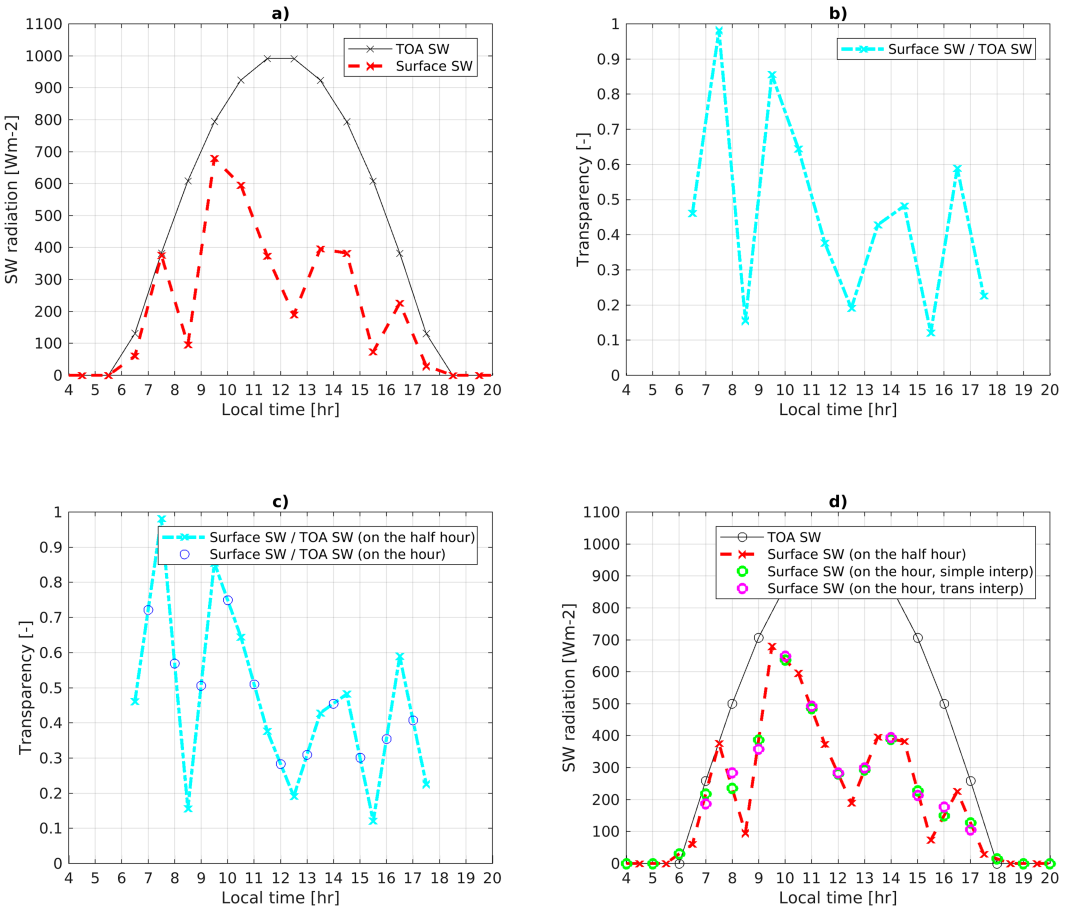

FIG. A1. Illustration of the four-step transformation of surface shortwave radiation data from hourly mean on the half-hour to hourly mean on the hour, over a diurnal cycle: (a) original radiation values hourly on the half-hour, (b) surface shortwave radiation scaled by TOA radiation (transparency), (c) comparison of transparency values on the hour and at half past the hour, and (d) comparison of hourly values using our methodology (in purple) with those using a simple time interpolation (in green).

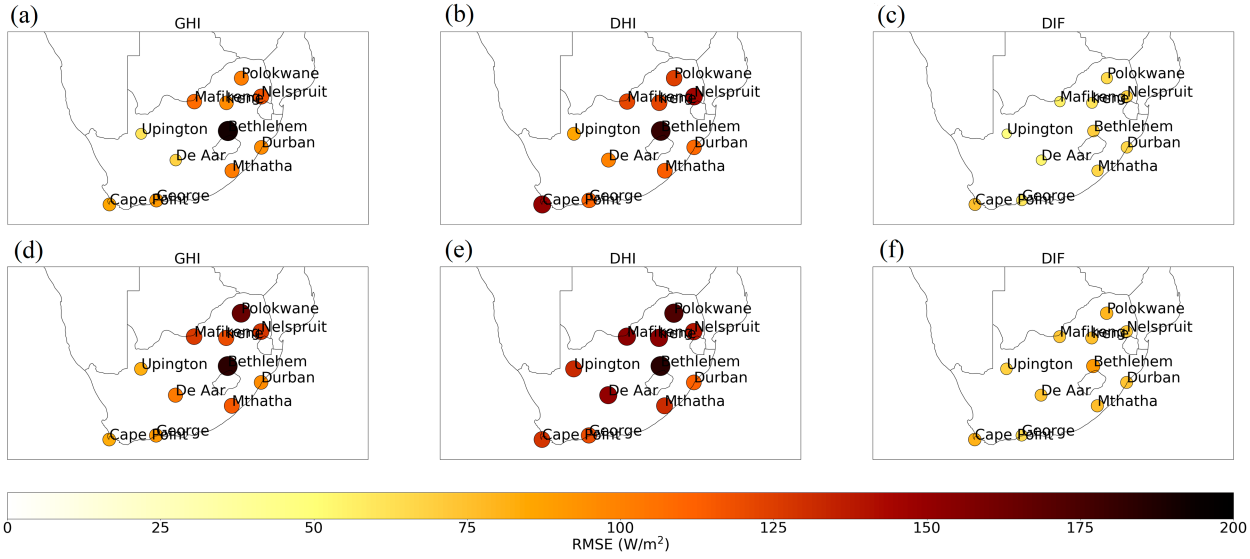

FIG. A2. Surface shortwave radiation RMSE (W m^{-2}) per location for (a) GHI SA4, (b) DHI SA4, (c) DIF SA4, (d) GHI SA1.5, (e) DHI SA1.5, and (f) DIF SA1.5.

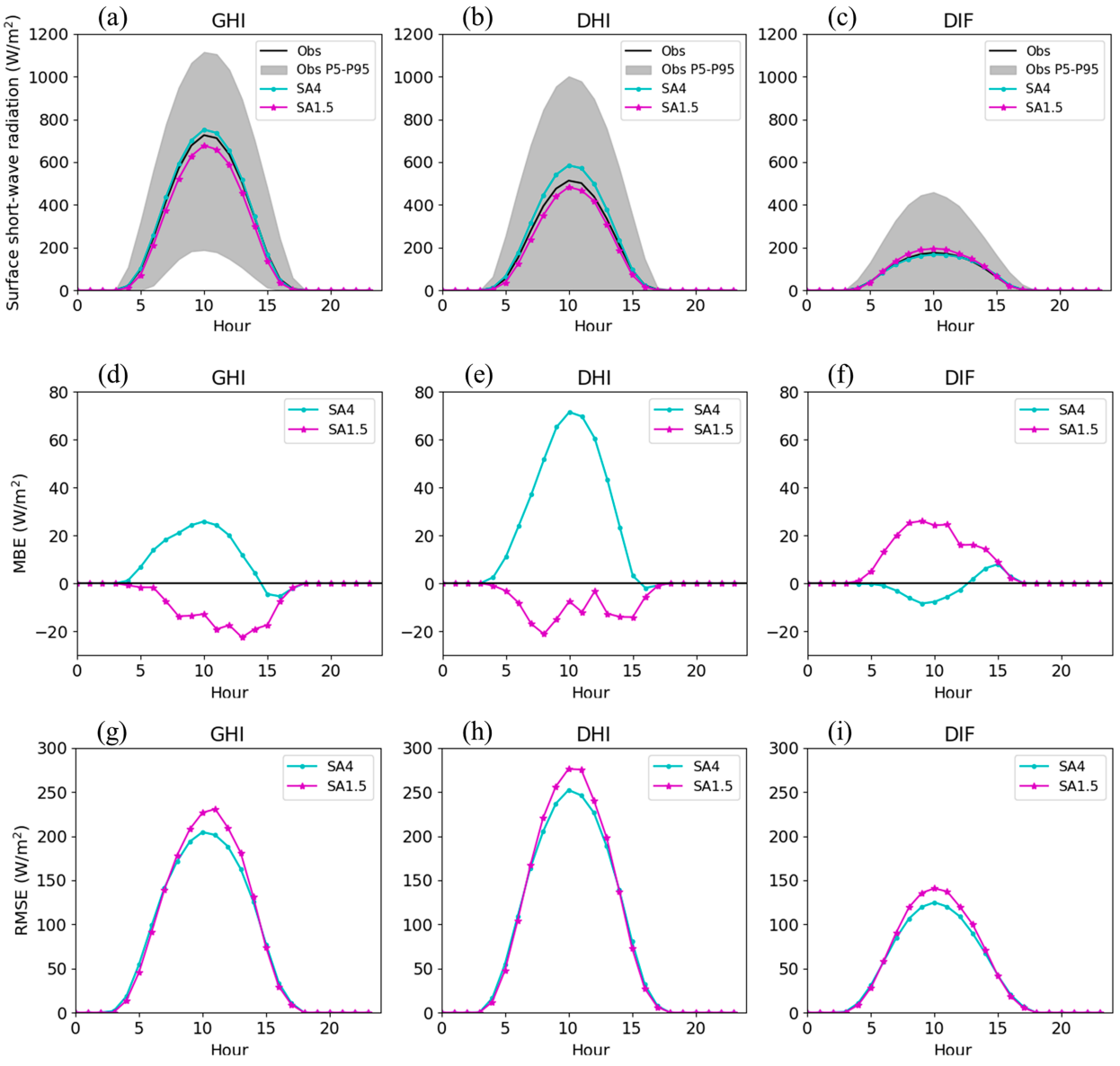

FIG. A3. Surface shortwave radiation diurnal cycles and errors (W m^{-2}) for SA4 and SA1.5, showing (a)–(c) diurnal cycles, with 5th–95th percentile range, (d)–(f) mean bias errors, and (g)–(i) RMSE for (left) GHI, (center) DHI, and (right) DIF.

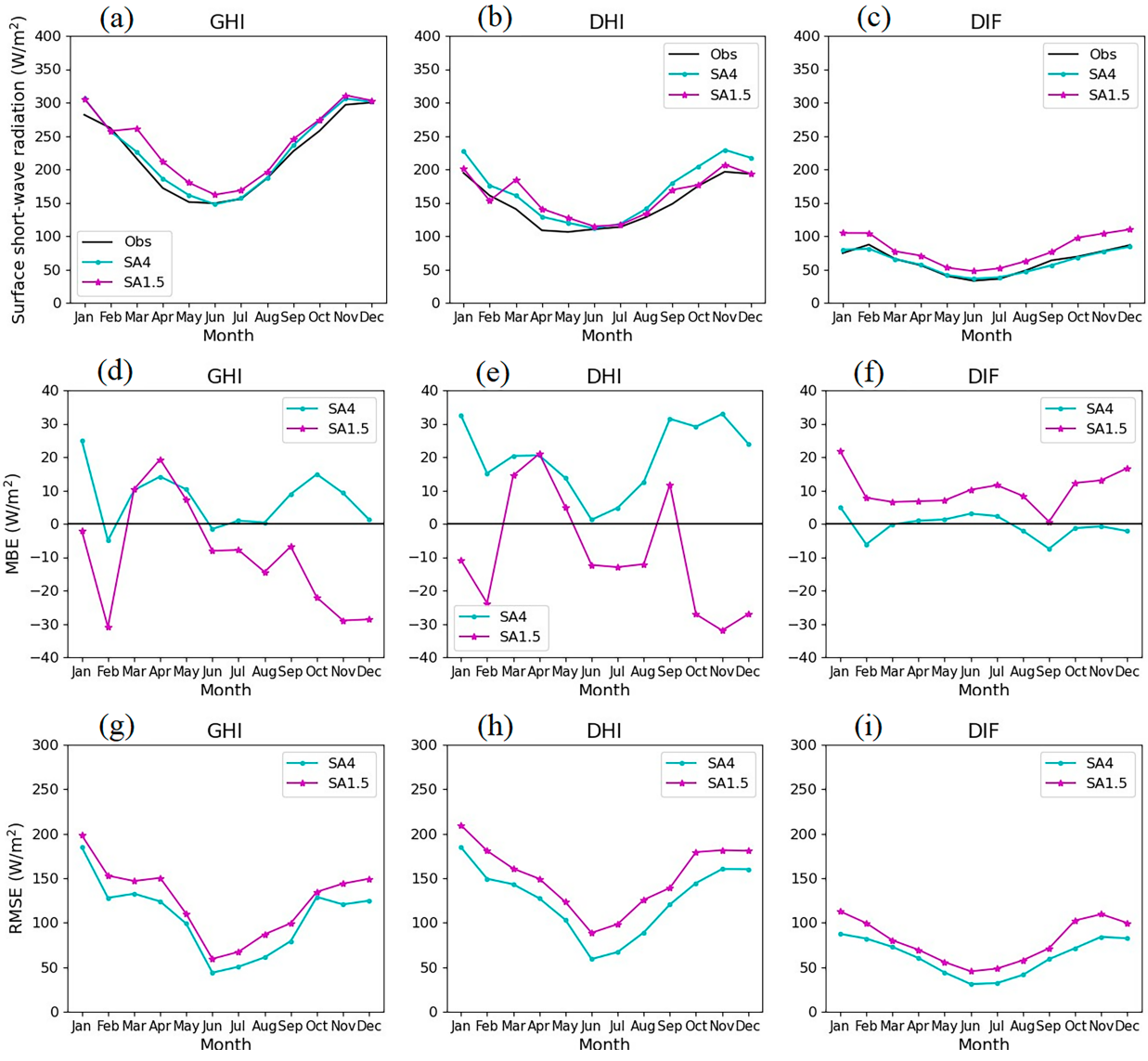

FIG. A4. As in Fig. A3, but for monthly cycles and errors.

TABLE A1. SA4 scaled surface shortwave radiation errors.

Radiation (unitless)	MBE	MAE	RMSE	R^2	SDE	P5	P50	P95
GHI	0.00	0.06	0.14	0.82	0.14	−0.19	0.00	0.20
DHI	0.02	0.07	0.14	0.70	0.14	−0.16	0.00	0.29
DIF	0.00	0.04	0.08	0.53	0.08	−0.14	0.00	0.12

TABLE A2. SA1.5 scaled surface shortwave radiation errors.

Radiation (unitless)	MBE	MAE	RMSE	R^2	SDE	P5	P50	P95
GHI	−0.01	0.07	0.15	0.79	0.15	−0.27	0.00	0.18
DHI	−0.01	0.08	0.16	0.61	0.16	−0.31	0.00	0.24
DIF	0.01	0.05	0.09	0.39	0.09	−0.13	0.00	0.17

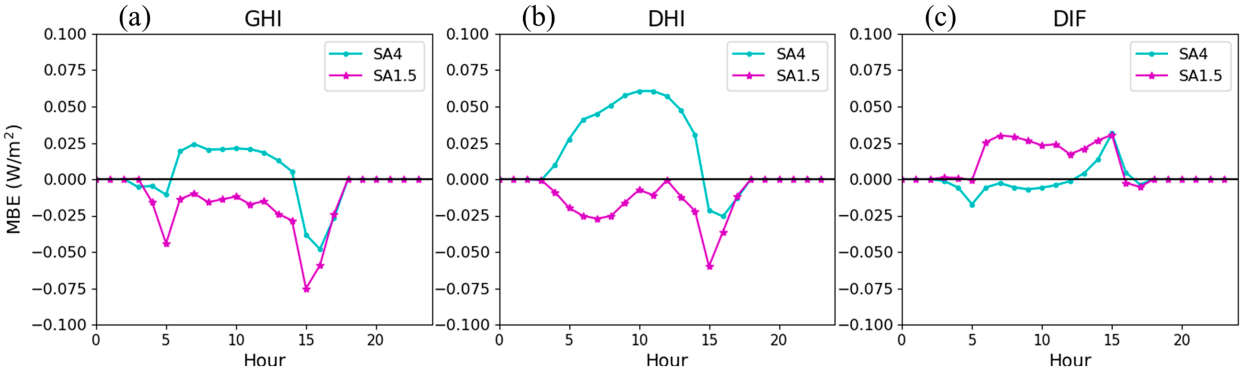

FIG. A5. Scaled surface shortwave radiation mean bias (unitless) per hour, for SA4 and SA1.5 for (a) GHI, (b) DHI, and (c) DIF.

TABLE A3. SA4 forecast results, as shown in Fig. 5.

Cloud fraction	0	0.125	0.25	0.375	0.5	0.625	0.75	0.875	1
Frequency (%)	36.06	7.60	3.27	3.02	2.87	2.97	3.78	13.14	27.30
GHI (W m^{-2})	321.24	361.80	365.54	368.16	348.26	325.65	348.83	343.11	159.52
Area (W m^{-2})	115.83	27.5	11.94	11.13	10.01	9.67	13.17	45.07	43.54
DHI (W m^{-2})	269.56	302.27	296.06	291.39	268.47	241.08	249.91	228.79	61.59
Area (W m^{-2})	97.20	22.98	9.67	8.81	7.72	7.16	9.44	30.05	16.81
DIF (W m^{-2})	51.68	59.52	69.48	76.77	79.79	84.57	98.92	114.32	97.94
Area (W m^{-2})	18.63	4.52	2.27	2.32	2.29	2.51	3.74	15.02	26.73

TABLE A4. SA4 observations results, as shown in Fig. 5.

Cloud fraction	0	0.125	0.25	0.375	0.5	0.625	0.75	0.875	1
Frequency (%)	30.18	13.95	10.45	7.48	6.94	6.33	6.84	10.63	7.19
GHI (W m^{-2})	254.63	364.28	356.93	370.65	357.42	335.18	274.16	165.9	94.14
Area (W m^{-2})	76.84	50.81	37.31	27.71	24.81	21.23	18.75	17.64	6.77
DHI (W m^{-2})	207.05	297.96	276.09	265.8	216.21	183.2	112.77	28.62	4.04
Area (W m^{-2})	62.48	41.56	28.86	19.87	15.01	11.6	7.71	3.04	0.29
DIF (W m^{-2})	38.58	55.43	68.72	93.77	129.63	143.72	149.32	114.79	60.62
Area (W m^{-2})	18.63	4.52	2.27	2.32	2.29	2.51	3.74	15.02	26.73

TABLE A5. SA1.5 forecast results, as shown in Fig. 5.

Cloud fraction	0	0.125	0.25	0.375	0.5	0.625	0.75	0.875	1
Frequency (%)	26.65	7.33	3.16	2.85	2.76	3.47	3.77	14.07	36.07
GHI (W m^{-2})	317.59	343.81	340.31	360.28	366.33	319.79	329.47	290.38	146.26
Area (W m^{-2})	84.62	25.29	10.74	10.28	10.11	10.70	12.42	40.85	52.76
DHI (W m^{-2})	260.40	282.02	271.40	282.06	276.80	233.76	229.17	170.09	38.07
Area (W m^{-2})	69.39	20.67	8.57	8.05	7.63	7.82	8.64	23.93	13.73
DIF (W m^{-2})	57.18	61.79	68.90	78.22	89.54	86.03	100.30	120.28	108.19
Area (W m^{-2})	15.24	4.53	2.18	2.23	2.47	2.88	3.78	16.92	39.03

TABLE A6. SA1.5 observations results, as shown in Fig. 5.

Cloud fraction	0	0.125	0.25	0.375	0.5	0.625	0.75	0.875	1
Frequency (%)	30.31	14.03	10.06	6.99	6.80	6.26	6.92	11.12	7.52
GHI (W m^{-2})	248.66	333.13	338.06	346.85	328.88	308.53	249.17	163.57	93.73
Area (W m^{-2})	75.36	46.73	34.02	24.25	22.35	19.31	17.25	18.19	7.05
DHI (W m^{-2})	200.06	269.15	259.10	243.44	195.18	162.81	97.35	27.37	3.69
Area (W m^{-2})	60.63	37.75	26.07	17.02	13.26	10.19	6.74	3.04	0.28
DIF (W m^{-2})	41.98	55.39	69.07	94.42	124.47	138.62	141.17	113.03	60.23
Area (W m^{-2})	12.72	7.77	6.95	6.60	8.46	8.68	9.77	12.57	4.52

APPENDIX B

Cloud Profile Observations (Per Hour and Month) and Errors (Per Location)

Figure B1 shows the observed cloud profiles for low- (0–3 km AGL), mid- (3–6 km AGL), and high-level (6–20 km AGL) clouds, aggregated for each of the available times of day (0600, 1200, and 1800 UTC), and by month. Cloud profiles do not exhibit strong diurnal or seasonal patterns. The prevalence of low-level clouds is observed throughout the day and year.

Figure B2 illustrates the RMSE for total cloud amount at each radiometric station, comparing SA4 and SA1.5 models. No geographical patterns in the errors were seen.

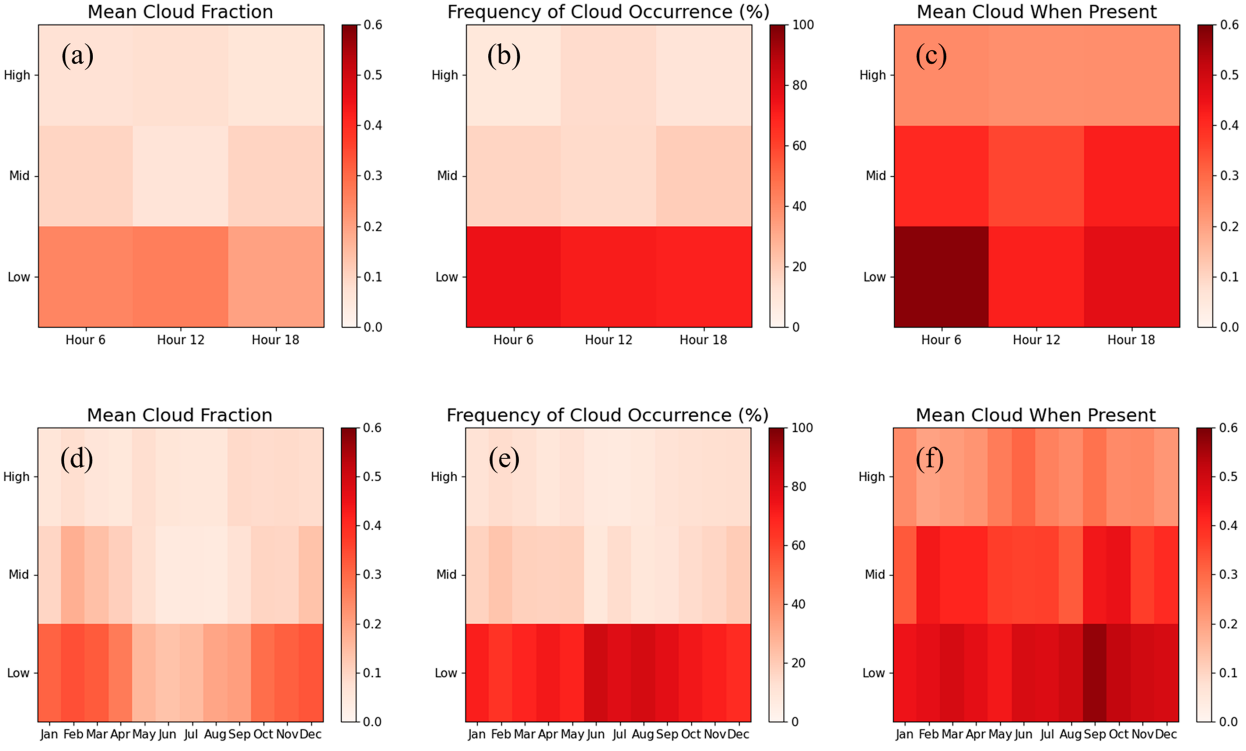

FIG. B1. Observed clouds aggregated by time of day and month, per level: low level (0–3 km AGL), midlevel (3–6 km AGL), high level (6–20 km AGL). Shown are (left) mean cloud fraction, (center) frequency of cloud excluding clear sky, and (right) mean cloud fraction when present (excluding clear sky) per (a)–(c) hour (as labeled) and (d)–(f) month.

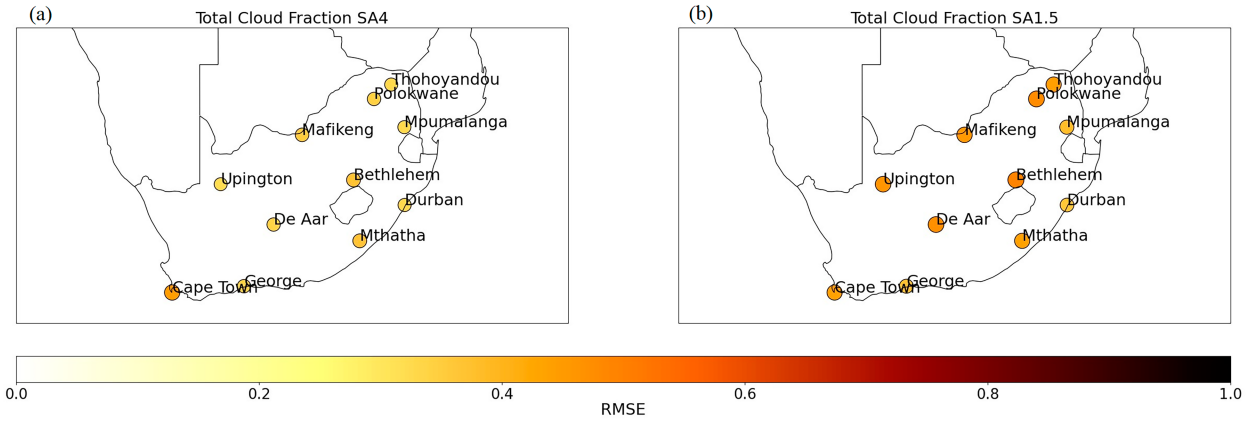

FIG. B2. Total cloud RMSE (unitless) per location for (a) SA4 and (b) SA1.5.

REFERENCES

Bush, M., and Coauthors, 2020: The first Met Office Unified Model–JULES Regional Atmosphere and Land configuration, RAL1. *Geosci. Model Dev.*, **13**, 1999–2029, https://doi.org/10.5194/gmd-13-1999-2020.

Clark, P., N. Roberts, H. Lean, S. P. Ballard, and C. Charlton-Perez, 2016: Convection-permitting models: A step-change in rainfall forecasting. *Meteor. Appl.*, **23**, 165–181, https://doi.org/10.1002/met.1538.

Department of Energy, 2018: Integrated Resource Plan 2018. Department of Energy Republic of South Africa Government Notice, 77 pp., https://www.energy.gov.za/IRP/irp-update-draft-report2018/IRP-Update-2018-Draft-for-Comments.pdf.

——, 2019: Integrated Resource Plan 2019. Department of Mineral Resources and Energy of South Africa Government Notice, 100 pp., https://www.energy.gov.za/files/docs/IRP%202019.pdf.

Edwards, J. M., and A. Slingo, 1996: Studies with a flexible new radiation code. I: Choosing a configuration for a large-scale model. *Quart. J. Roy. Meteor. Soc.*, **122**, 689–719, https://doi.org/10.1002/qj.49712253107.

Govender, P., and V. Sivakumar, 2019: Investigating diffuse irradiance variation under different cloud conditions in Durban, using *k*-means clustering. *J. Energy S. Afr.*, **30**, 22–32, https://doi.org/10.17159/2413-3051/2019/v30i3a6314.

Jensen, M. P., and Coauthors, 2016: The Midlatitude Continental Convective Clouds Experiment (MC3E). *Bull. Amer. Meteor. Soc.*, **97**, 1667–1686, https://doi.org/10.1175/BAMS-D-14-00228.1.

Jiang, B., and Coauthors, 2015: Empirical estimation of daytime net radiation from shortwave radiation and ancillary information. *Agric. For. Meteor.*, **211–212**, 23–36, https://doi.org/10.1016/j.agrformet.2015.05.003.

Keat, W. J., and Coauthors, 2019: Convective initiation and storm life cycles in convection-permitting simulations of the Met Office Unified Model over South Africa. *Quart. J. Roy. Meteor. Soc.*, **145**, 1323–1336, https://doi.org/10.1002/qj.3487.

Kendon, E., E. M. Fischer, and C. J. Short, 2023: Variability conceals emerging trend in 100yr projections of UK local hourly rainfall extremes. *Nat. Commun.*, **14**, 1133, https://doi.org/10.1038/s41467-023-36499-9.

Lean, H. W., P. A. Clark, M. Dixon, N. M. Roberts, A. Fitch, R. Forbes, and C. Halliwell, 2008: Characteristics of high-resolution versions of the Met Office Unified Model for forecasting convection over the United Kingdom. *Mon. Wea. Rev.*, **136**, 3408–3424, https://doi.org/10.1175/2008MWR2332.1.

Long, C. N., and E. G. Dutton, 2010: BSRN Global Network recommended QC tests, V2.0. 3 pp., https://epic.awi.de/id/eprint/30083/1/BSRN_recommended_QC_tests_V2.pdf.

——, T. P. Ackerman, K. L. Gaustad, and J. N. S. Cole, 2006: Estimation of fractional sky cover from broadband shortwave radiometer measurements. *J. Geophys. Res.*, **111**, D11204, https://doi.org/10.1029/2005JD006475.

Mabasa, B., J. Botai, and L. Ntsangwane, 2018: Update on the re-establishment of the South African Weather Services (SAWS) radiometric network in all six climatological regions and the quality of the data. *Proc. Fifth South African Solar Energy Conf. (SASEC)*, Durban, South Africa, Centre for Renewable and Sustainable Energy Studies, https://www.sasec.org.za/full_papers/68.pdf.

——, H. Tazvinga, N. Zwane, J. Botai, and L. Ntsangwane, 2019: Assessment of Global Horizontal Irradiance in South Africa. *Proc. Sixth South African Solar Energy Conf. (SASEC)*, East London, South Africa, Centre for Renewable and Sustainable Energy Studies, https://www.sasec.org.za/papers2019/47.pdf.

——, M. D. Lysko, H. Tazvinga, S. T. Mulaudzi, N. Zwane, and S. J. Moloi, 2020: The Ångström–Prescott regression coefficients for six climatic zones in South Africa. *Energies*, **13**, 5418, https://doi.org/10.3390/en13205418.

——, ——, and S. J. Moloi, 2021: Validating hourly satellite based and reanalysis based global horizontal irradiance datasets over South Africa. *Geomatics*, **1**, 429–449, https://doi.org/10.3390/geomatics1040025.

Manners, J., J. M. Edwards, P. Hill, and J.-C. Thelen, 2018: SOCRATES Technical Guide: Suite of Community Radiative Transfer Codes Based on Edwards and Slingo. Met Office, 87 pp., https://homepages.see.leeds.ac.uk/~lecsjed/winscpuse/socrates_techguide.pdf.

Matuszko, D., 2012: Influence of the extent and genera of cloud cover on solar radiation intensity. *Int. J. Climatol.*, **32**, 2403–2414, https://doi.org/10.1002/joc.2432.

Mittermaier, M., 2012: A critical assessment of surface cloud observations and their use for verifying cloud forecasts. *Quart. J. Roy. Meteor. Soc.*, **138**, 1794–1807, https://doi.org/10.1002/qj.1918.

Morcrette, C. J., E. J. O'Connor, and J. C. Petch, 2012: Evaluation of two cloud parametrization schemes using ARM and

Cloud-Net observations. *Quart. J. Roy. Meteor. Soc.*, **138**, 964–979, https://doi.org/10.1002/qj.969.

Schär, C., and Coauthors, 2020: Kilometer-scale climate models: Prospectives and challenges. *Bull. Amer. Meteor. Soc.*, **101**, E567–E587, https://doi.org/10.1175/BAMS-D-18-0167.1.

Singh, J., 2016: Ranking South African provinces on the basis of MERRA 2D surface incident shortwave flux. *J. Energy South. Afr.*, **27**, 50–57, https://doi.org/10.17159/2413-3051/2016/v27i3a1555.

——, and A. Kruger, 2017: Is the summer season losing potential for solar energy applications in South Africa? *J. Energy South. Afr.*, **28**, 52–60, https://doi.org/10.17159/2413-3051/2017/v28i2a1673.

Smith, R. N. B., 1990: A scheme for predicting layer clouds and their water content in a general circulation model. *Quart. J. Roy. Meteor. Soc.*, **116**, 435–460, https://doi.org/10.1002/qj.49711649210.

Stein, T. H. M., and Coauthors, 2019: An evaluation of clouds and precipitation in convection-permitting forecasts for South Africa. *Wea. Forecasting*, **34**, 233–254, https://doi.org/10.1175/WAF-D-18-0080.1.

Tazvinga, H., M. Thopil, P. B. Numbi, and T. Adefarati, 2017: Distributed renewable energy technologies. *Handbook of Distributed Generation: Electric Power Technologies, Economics and Environmental Impacts*, Springer, 3–67, https://doi.org/10.1007/978-3-319-51343-0_1.

Van Weverberg, K., and C. J. Morcrette, 2022: Sensitivity of cloud-radiative effects to cloud fraction parameterizations in tropical, midlatitude, and Arctic kilometre-scale simulations. *Quart. J. Roy. Meteor. Soc.*, **148**, 2563–2586, https://doi.org/10.1002/qj.4325.

——, ——, H.-Y. Ma, S. A. Klein, and J. C. Petch, 2015: Using regime analysis to identify the contribution of clouds to surface temperature errors in weather and climate models. *Quart. J. Roy. Meteor. Soc.*, **141**, 3190–3206, https://doi.org/10.1002/qj.2603.

——, I. A. Boutle, C. J. Morcrette, and R. K. Newsom, 2016: Towards retrieving critical relative humidity from ground-based remote-sensing observations. *Quart. J. Roy. Meteor. Soc.*, **142**, 2867–2881, https://doi.org/10.1002/qj.2874.

——, and Coauthors, 2018: CAUSES: Attribution of surface radiation biases in NWP and climate models near the U.S. Southern Great Plains. *J. Geophys. Res. Atmos.*, **123**, 3612–3644, https://doi.org/10.1002/2017JD027188.

——, C. J. Morcrette, and I. A. Boutle, 2021: A bimodal diagnostic cloud fraction parameterization. Part II: Evaluation and resolution sensitivity. *Mon. Wea. Rev.*, **149**, 859–878, https://doi.org/10.1175/MWR-D-20-0230.1.

Walters, D. N., and Coauthors, 2011: The Met Office Unified Model global atmosphere 3.0/3.1 and JULES global land 3.0/3.1 configurations. *Geosci. Model Dev.*, **4**, 919–941, https://doi.org/10.5194/gmd-4-919-2011.

Webster, S., M. Uddstrom, H. Oliver, and S. Vosper, 2008: A high-resolution modelling case study of a severe weather event over New Zealand. *Atmos. Sci. Lett.*, **9**, 119–128, https://doi.org/10.1002/asl.172.

Wilson, D. R., A. C. Bushell, A. M. Kerr-Munslow, J. D. Price, and C. J. Morcrette, 2008: PC2: A prognostic cloud fraction and condensation scheme. I: Scheme description. *Quart. J. Roy. Meteor. Soc.*, **134**, 2093–2107, https://doi.org/10.1002/qj.333.

WMO, 2013: Baseline Surface Radiation Network (BSRN): Update of the technical plan for BSRN data management. GCOS-174, 30 pp., https://library.wmo.int/doc_num.php?explnum_id=7198.

——, 2017: Guide to Meteorological Instruments and Methods of Observation. WMO-8, 681 pp., https://www.weather.gov/media/epz/mesonet/CWOP-WMO8.pdf.

——, 2018: Meteorological Service for International Air Navigation. Technical Regulations, Vol. II, WMO-49, 206 pp., https://library.wmo.int/viewer/35795/.

——, 2019: General Meteorological Standards and Recommended Practices. Technical Regulations, Vol. I, WMO-49, 71 pp., https://library.wmo.int/doc_num.php?explnum_id=10113.

Zhang, X., S. Liang, G. Zhou, H. Wu, and X. Zhao, 2014: Generating global land surface satellite incident shortwave radiation and photosynthetically active radiation products from multiple satellite data. *Remote Sens. Environ.*, **152**, 318–332, https://doi.org/10.1016/j.rse.2014.07.003.